Supplementary Information

Exploring van der Waals materials with high anisotropy: geometrical and optical approaches

Aleksandr S. Slavich[1,†],Georgy A. Ermolaev[2,†], Mikhail K. Tatmyshevskiy[1], Adilet N. Toksumakov[1], Olga G. Matveeva[1], Dmitriy V. Grudinin[2], Arslan Mazitov[4], Konstantin V. Kravtsov[1], Alexander V. Syuy[2], Dmitry M. Tsymbarenko[3], Mikhail S. Mironov[2], Sergey M. Novikov[1], Ivan Kruglov[2], Davit A. Ghazaryan[1,5], Andrey A. Vyshnevyy[2], Aleksey V. Arsenin[2,5], Valentyn S. Volkov[2,5], and Kostya S. Novoselov[6,7,8,]*

[1]*Moscow Center for Advanced Studies, Kulakova str. 20, Moscow, 123592, Russia*

[2]*Emerging Technologies Research Center, XPANCEO, Internet City, Emmay Tower, Dubai, United Arab Emirates*

[3]*Department of Chemistry, Lomonosov Moscow State University, Moscow, 119991, Russia*

[4]*Institute of Materials, École Polytechnique Fédérale de Lausanne, 1015 Lausanne, Switzerland*

[5]*Laboratory of Advanced Functional Materials, Yerevan State University, Yerevan 0025, Armenia*

[6]*National Graphene Institute (NGI), University of Manchester, Manchester, M13 9PL, UK*

[7]*Department of Materials Science and Engineering, National University of Singapore, Singapore, 03-09 EA, Singapore*

[8]*Chongqing 2D Materials Institute, 400714, Chongqing, China*

[†]These authors contributed equally to this work

**Correspondence should be addressed to: kostya@nus.edu.sg*

Table of Contents

Supplementary Note 1: Characterization of As_2S_3 flakes

Supplementary Table 1. Summary of the crystal structure and refinement details for As_2S_3.

Formula	As_2S_3
Formula weight	246.02
Diffractometer	Bruker D8 QUEST
Data collection method	ω scans
Temperature (K)	297(2)
Crystal system	Monoclinic
Space group	*P 2₁/n*
a (Å)	4.2546(4)
b (Å)	9.5775(10)
c (Å)	11.4148(10)
α (°)	90
β (°)	90.442(4)
γ (°)	90
V (Å^3)	465.12(8)
Z	4
Colour, habit	yellow, plate
Crystal dimensions (mm)	0.169 × 0.151 × 0.015
Density D_{calc} (g·cm^{-3})	3.513
μ (mm^{-1})	15.511
Unique reflections (R_{int})	1337 (0.0705)
Observed reflections [$I > 2\sigma(I)$]	1018
Parameters	46
$R_1[I > 2\sigma(I)]$, ωR_2	0.0480, 0.1258
Goodness of fit on F^2	1.057
Absorption correction	numerical
T_{min}, T_{max}	0.2170, 0.9763
ρ_{min}, ρ_{max} (eÅ^{-3})	-0.799, 2.353

Supplementary Table 2. Interatomic distances (Å) and bond angles (°) in As_2S_3 structure. Symmetry codes: (i) 1+x, y, z; (ii) -0.5+x, 0.5 - y, 0.5+z; (v) -1+x, y, z; (vi) 0.5+x, 0.5-y, -0.5+z.

Parameter	Distance	Parameter	Angle
As1−S1	2.2616(17)	S1−As1−S2^{i}	99.24(6)
As1−S2^{i}	2.2760(19)	S1−As1−S3	104.15(6)
As1−S3	2.2900(17)	S2^{i}−As1−S3	94.50(7)
As2−S1	2.2484(18)	S1−As2−S2	98.83(6)
As2−S2	2.2844(17)	S1−As2−S3^{ii}	92.67(6)
As2−S3^{ii}	2.2926(17)	S2−As2−S3^{ii}	104.98(6)
		As2−S1−As1	103.62(7)
		As1^{v}−S2−As2	100.84(7)
		As1−S3−As2^{vi}	87.98(6)

Supplementary Table 3. Unit cell parameters and atomic position in crystal structure of As_2S_3.

	This work	Work[1]	Work[2]
a (Å)	4.2546(4)	4.22(5)	4.256(2)
b (Å)	9.5775(10)	9.57(2)	9.577(4)
c (Å)	11.4148(10)	11.46(4)	11.475(5)
β (°)	90.442(4)	90.5(5)	90.41(5)
As1	x = 0.86181(16) y = 0.19139(7) z = 0.26514(5)	0.857 0.190 0.267	0.86274(41) 0.19171(22) 0.26469(15)
As2	x = 0.36056(16) y = 0.32129(7) z = 0.48652(5)	0.357 0.323 0.484	0.36072(41) 0.32122(22) 0.48677(15)
S1	x = 0.5099(4) y = 0.12111(18) z = 0.40041(13)	0.500 0.120 0.395	0.50811(98) 0.12128(47) 0.40151(39)
S2	x = 0.0115(4) y = 0.39755(18) z = 0.34757(13)	0.987 0.397 0.355	0.01011(105) 0.39723(51) 0.34738(39)
S3	x = 0.5603(4) y = 0.29344(18) z = 0.12185(13)	0.590 0.293 0.125	0.55896(96) 0.29354(48) 0.12234(37)
R_1 for all reflections	0.0652	0.18	0.089

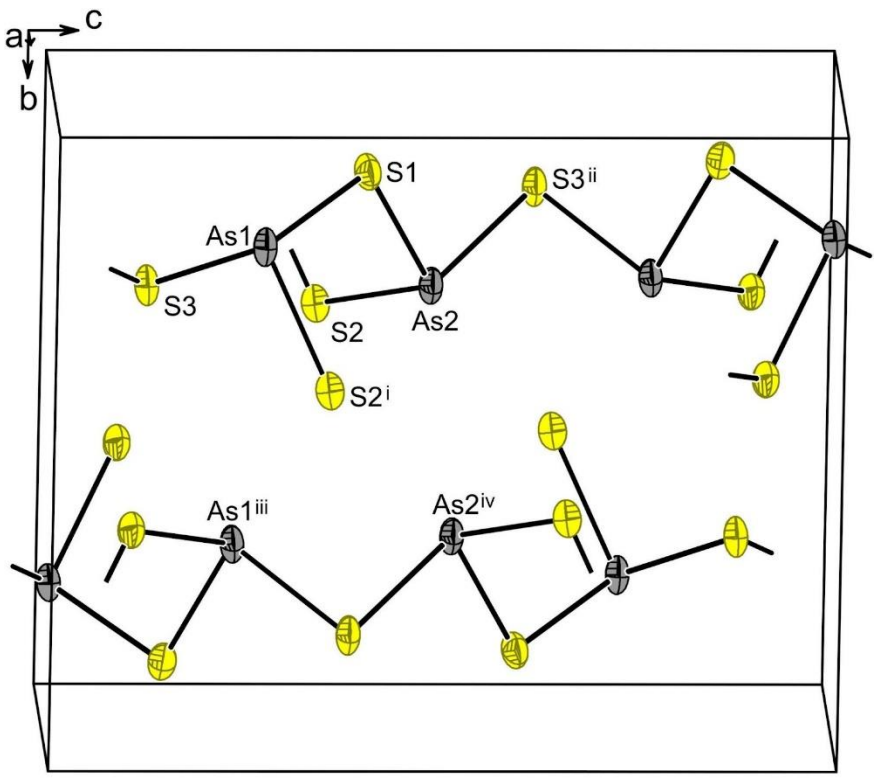

Supplementary Figure 1. X-ray crystal structure of As_2S_3. Thermal ellipsoids correspond to 50% probability. Symmetry codes: (i) 1+x, y, z; (ii) -0.5+x, 0.5 - y, 0.5+z; (iii) 1.5-x, 0.5+y, 0.5-z; (iv) 1-x, 1-y, 1-z.

To verify the single-crystalline nature of As_2S_3 thin flakes we perform transmission electron microscopy (TEM) analysis. Supplementary Figure 2a shows an optical image of an as-transferred As_2S_3 flake on SiN membrane. Supplementary Figure 2b demonstrates the selected area electron diffraction (SAED) pattern of the As_2S_3 at the same flake. To confirm the As_2S_3 structure SAED pattern simulations were performed using the lattice parameters obtained from our X-ray diffraction result. The simulated SAED pattern for the [010] projection of As_2S_3 (Supplementary Figure 2b) shows excellent agreement with experimental data. Energy-dispersive X-ray spectroscopy (EDX) measurements were further carried out to investigate the elemental composition of the specimen. The quantitative EDX analysis demonstrated a sufficient atomic stoichiometry As:S ≈ 38.1:61.9 as shown in Supplementary Figure 1c. The obtained results confirmed the expected structure and high purity of the exfoliated As_2S_3 thin flakes.

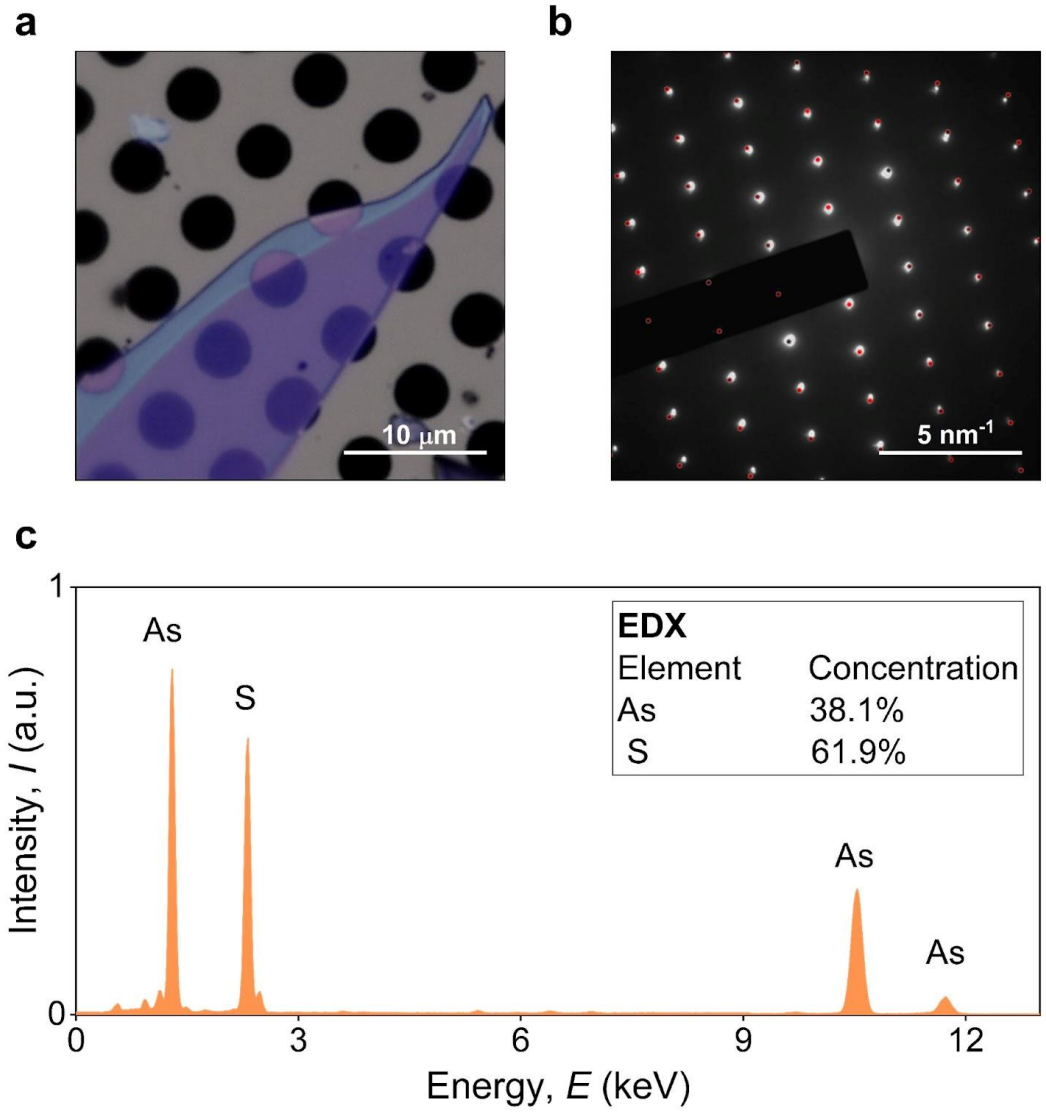

Supplementary Figure 2. As_2S_3 TEM characterization. (a) Optical image of mechanically exfoliated As_2S_3 sheet transferred over holey SiN membrane. (b) Experimental selected area electron diffraction pattern across ac crystallographic plane. Colored dots indicate Miller index simulation pattern. (c) Energy-dispersive X-ray spectrum (EDX) of the transferred As_2S_3 flake.

Supplementary Note 2: First-principle calculations

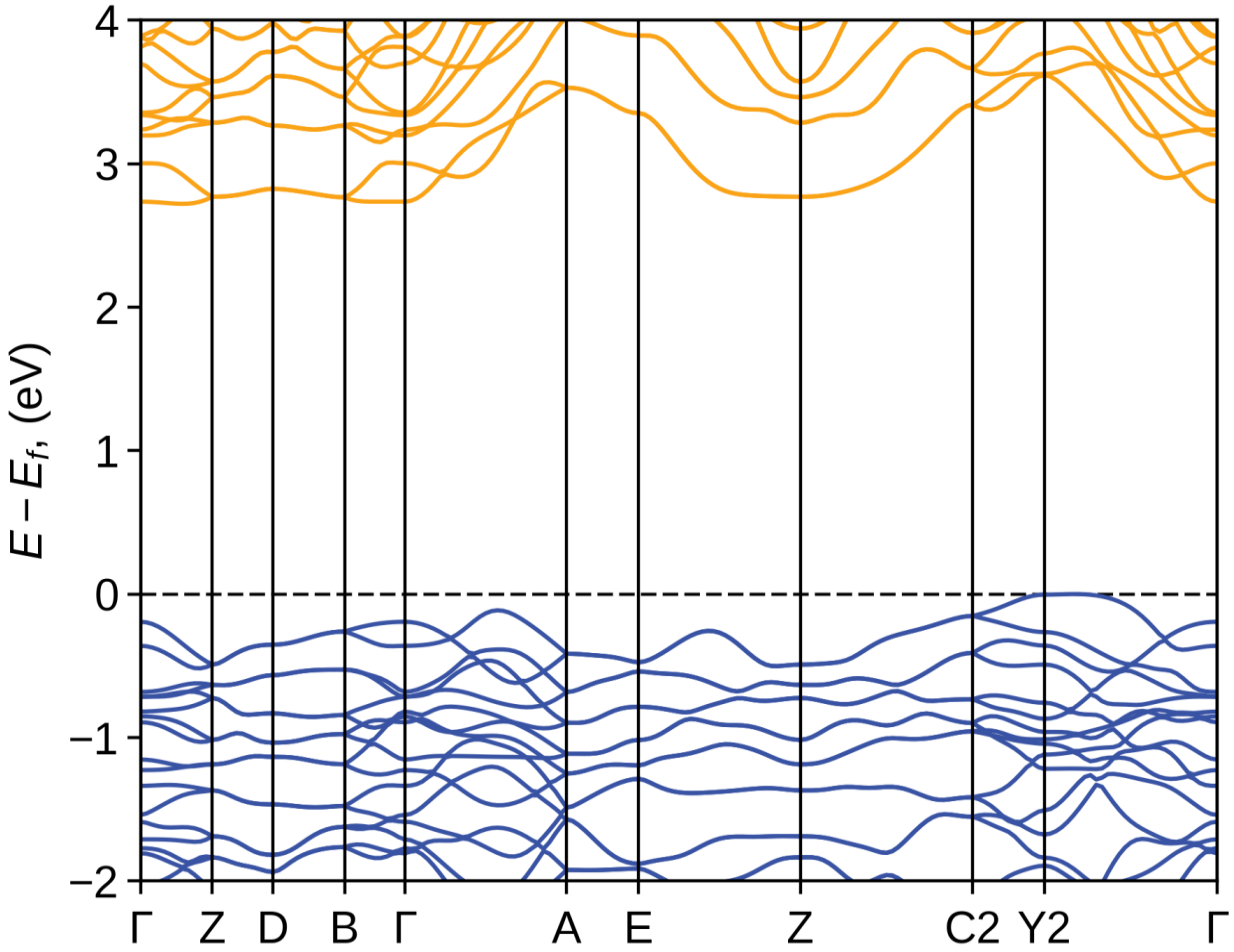

Supplementary Figure 3. Bandstructure of As_2S_3 calculated within HSE06 hybrid functional using VASP code.

Optical properties of As_2S_3 were calculated within PBE[3], HSE06[4], PBE+GW[5,6] and HSE06+GW[7] approximations using the VASP code. In the GW approach, macro- and micro-dielectric tensors were also calculated. The comparison of different methods is shown in Supplementary Figure 4. As expected, the best match between experiment and theory (Supplementary Figure 4j) was for GW+HSE06 approach and micro-dielectric tensor for in-plane optical properties, and macro-dielectric tensor for out-of-plane optical properties.

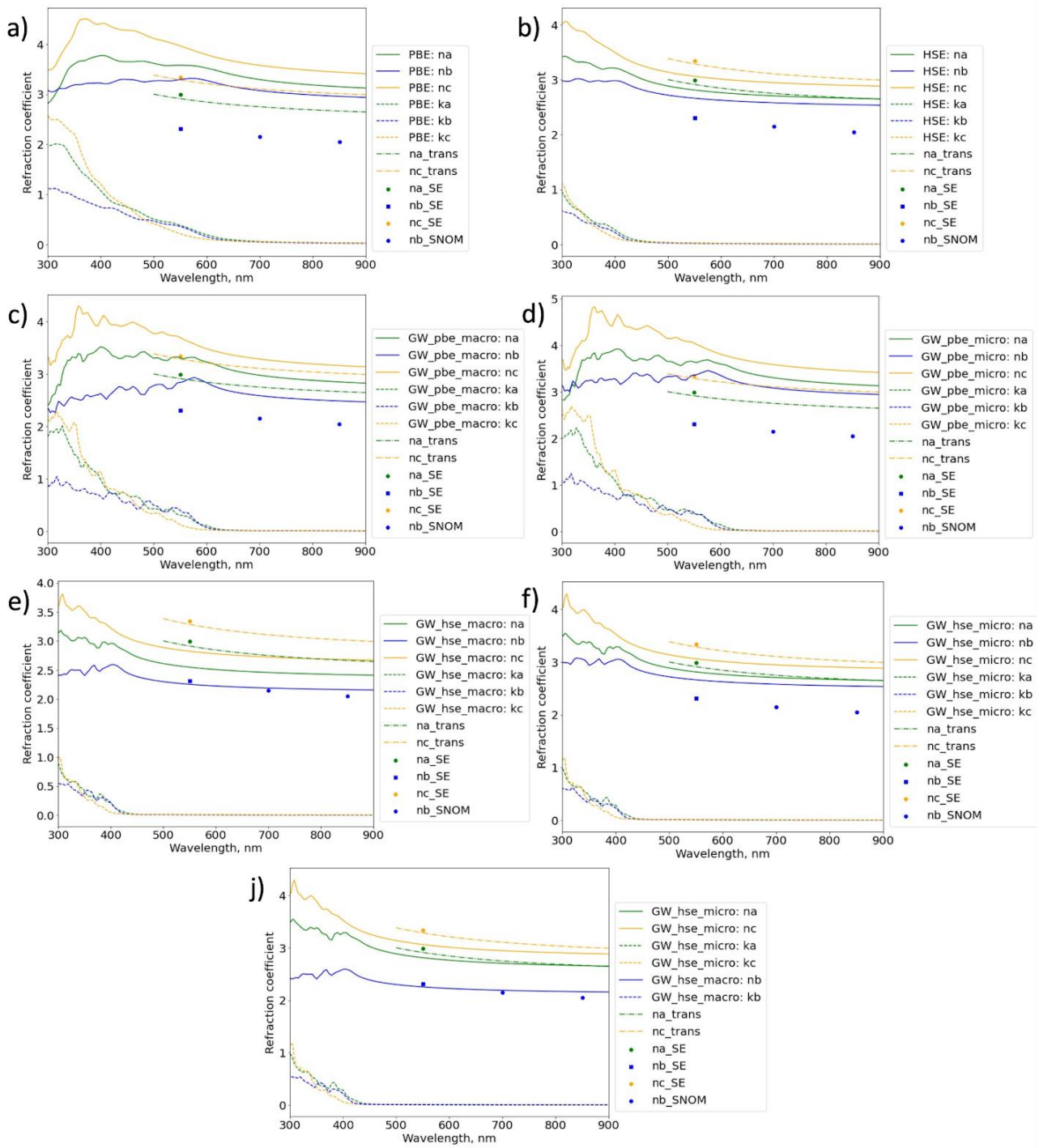

Supplementary Figure 4. Optical properties of As_2S_3 calculated within a) PBE, b) HSE06, c) GW+PBE (from macro dielectric tensor), d) GW+PBE (from micro dielectric tensor), e) GW+HSE06 (from macro dielectric tensor), f) GW+HSE06 (from micro dielectric tensor), j) mixed micro-GW+HSE06 for in-plane and macro-GW+HSE06 for out-of-plane constants. Theoretically calculated data for refractive index is shown with solid line, experimental data - with dotted lines and points.

Supplementary Note 3: Polarization-dependent Raman spectroscopy

Lattice dynamics calculations of As_2S_3 were performed using the Phonopy[8,9] and Phono3py[10] codes, where VASP[11] was used to calculate interatomic forces. Calculations were performed in the generalized form of gradient approximation (GGA), parametrized by the PBE exchange-correlation functional[3] along with Grimme-D3 scheme[12] to account for van der Waals interactions. For modeling ionic cores the PAW pseudopotentials[13,14] were used treating the As 4s and 4p and the S 3s and 3p electrons as valence. A kinetic energy cutoff for the plane wave basis set was set to 350 eV. k-meshes of 12×5×4 and 4×3×4 subdivisions were used for the As_2S_3 primitive cell and supercells, respectively. The second-order force constants were calculated for 3×2×1 supercell (120 atoms) with a finite displacement step of 0.01 Å. A tolerance of 10^{-8} eV was set for total-energy calculations. We also considered a non-analytical term correction (NAC)[15–17] for dynamical matrix to account for long-range dipole-dipole interactions.

Intensities of Raman peaks were calculated using the VASP package for both PBE and HSE06 functionals[4]. We used a default value of screening parameter = 0.2 for HSE06 with 25% mixing of exact exchange. For a static dielectric matrix and Born effective charges calculations a DFPT was used as implemented in VASP in the case of PBE. Finite electric field approach was used in the case of HSE06 with 0.002 eV/Å being the value of the applied electric field allowing one to avoid onset Zener tunneling in consistency with an evaluated band gap of 2.71 eV.

Linewidths were estimated using the Phono3py code. The third-order force constants were calculated for 3×2×1 supercell with atomic displacement of 0.03 Å. During post processing, the phonon lifetimes were sampled on regular Gamma-centered 21×21×21 q-point meshes.

A space group of As_2S_3 is P 2_1/n (monoclinic crystal system), therefore Raman active modes are A_g and B_g[15-16]. To compute polarized Raman spectra (Supplementary Figure 5) we select only A_g modes with consistency with the experiment: backscattering geometry (laser beam parallel to b-axis) and parallel configuration (polarizer parallel to analyzer). Supplementary Figure 5 shows the calculated Raman spectra for incident laser-beam polarization along two crystalline axes and intensities of Raman-active modes as a function of polarization angle. Note, that the orientations of A_g^1–A_g^{10} patterns are fixed relative to in-plane crystallographic directions. So the evaluated polar diagrams could be used to estimate directions of crystallographic axes in real experiment. As_2S_3 flakes used in this study were exfoliated onto a Schott glass and silicon substrates. Supplementary Figures 6-7 show optical and atomic force microscopy (AFM) images of 60-nm-thick and 310-nm-thick As_2S_3 flakes. For the measurements of Raman spectra of the studied samples, Horiba LabRAM HR Evolution confocal scanning Raman microscope (Horiba Ltd., Kyoto, Japan) was used. All measurements were carried out using linearly polarized excitation of a 632.8 nm helium-neon laser. The studied samples were placed on a rotating table, which allowed us to measure angle-resolved Raman spectra. The Raman spectra were acquired at a range of angles from 0° to 360° with normal incidence angle by rotating a sample with a 5° step for 60-nm-thick As_2S_3 flake and with a 10° step for 310-nm-thick As_2S_3 flake. Supplementary Figures 8-9 show the

comparison of the polarized Raman modes intensities of the bulk As_2S_3 crystals with calculated data. Unfortunately, some peaks we cannot reliably resolve in terms of its polar diagram because of low peak intensity or small distance between peaks in experiment. However, it is clearly seen that calculated polar diagrams for the A_g^2, A_g^4-A_g^6 and A_g^9 modes are in excellent agreement with the experimental data. Therefore, these modes can be used to determine the crystalline axes of As_2S_3.

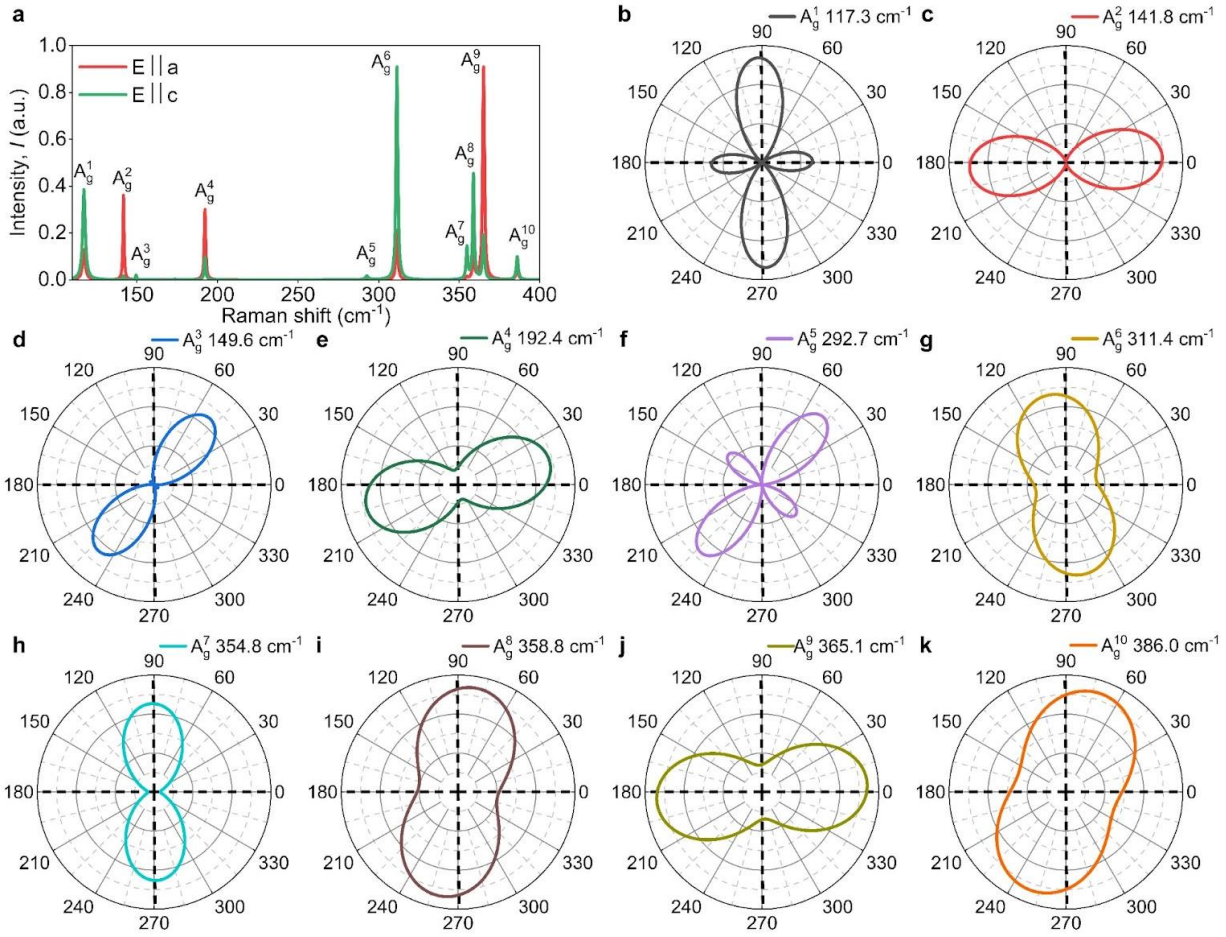

Supplementary Figure 5. Raman spectra of As_2S_3 from first-principle calculations. (a) Calculated Raman spectra along *a*-axis and *c*-axis evaluated with polarizer being parallel to analyzer. (b-k) Polar diagrams for A_g modes. Dashed lines indicate crystallographic axes directions: 0° corresponds to *a*-axis while 90.442° to *c*-axis.

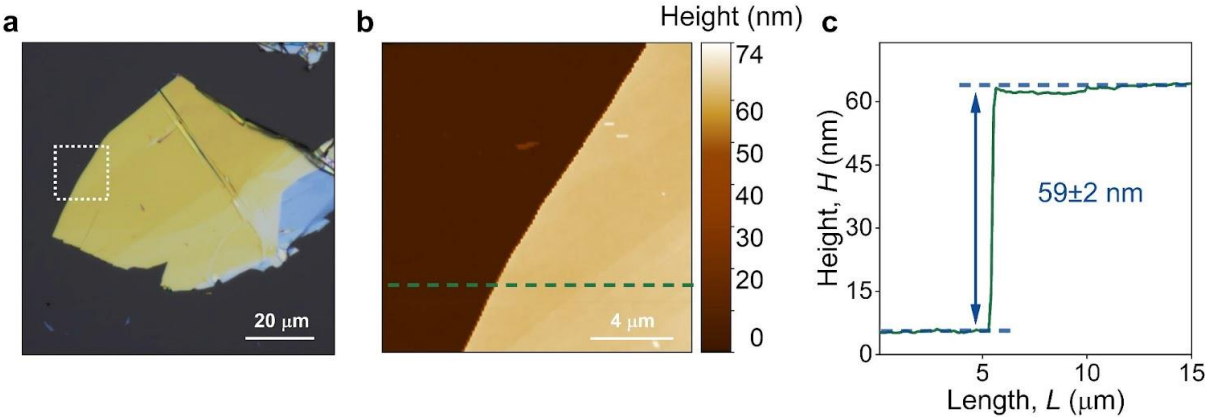

Supplementary Figure 6. AFM characterization of the As_2S_3 flake ($t \approx 60$ nm). (a) Optical image of the As_2S_3 flake on Schott glass. (b) AFM image outlined in (a). (c) Cross-section analysis along the green dashed line in (b).

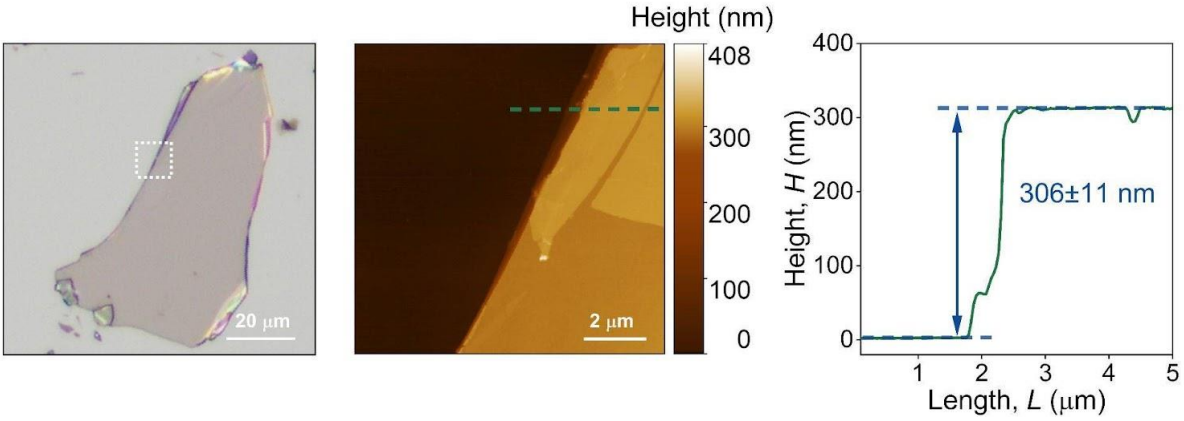

Supplementary Figure 7. AFM analysis of the As_2S_3 flake exfoliated on silicon ($t \approx 310$ nm). (a) Optical image of the As_2S_3 flake on Si. (b) AFM micrograph defined in (a). (c) Step height profile along the green dashed line in (b).

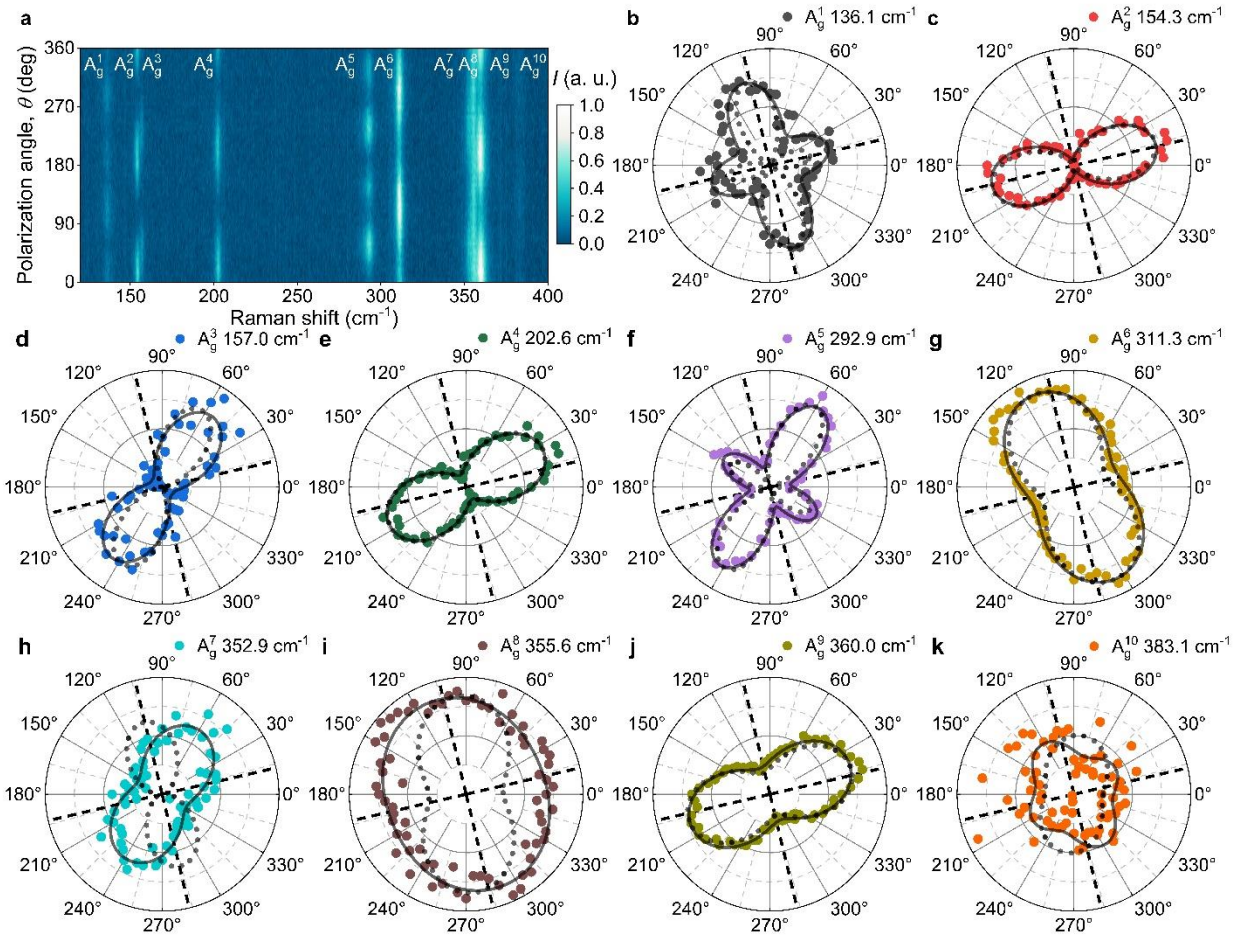

Supplementary Figure 8. (a) Experimental Raman spectra of thin As_2S_3 ($t \approx 60$nm) exfoliated on Schott glass. (b-k) Polar plots of the fitted peak intensities for ten Raman modes. Grey dotted curves correspond to Raman calculations. The data in polar diagrams are normalized to their maximum values, respectively. Dashed lines indicate *a* and *c* crystallographic directions.

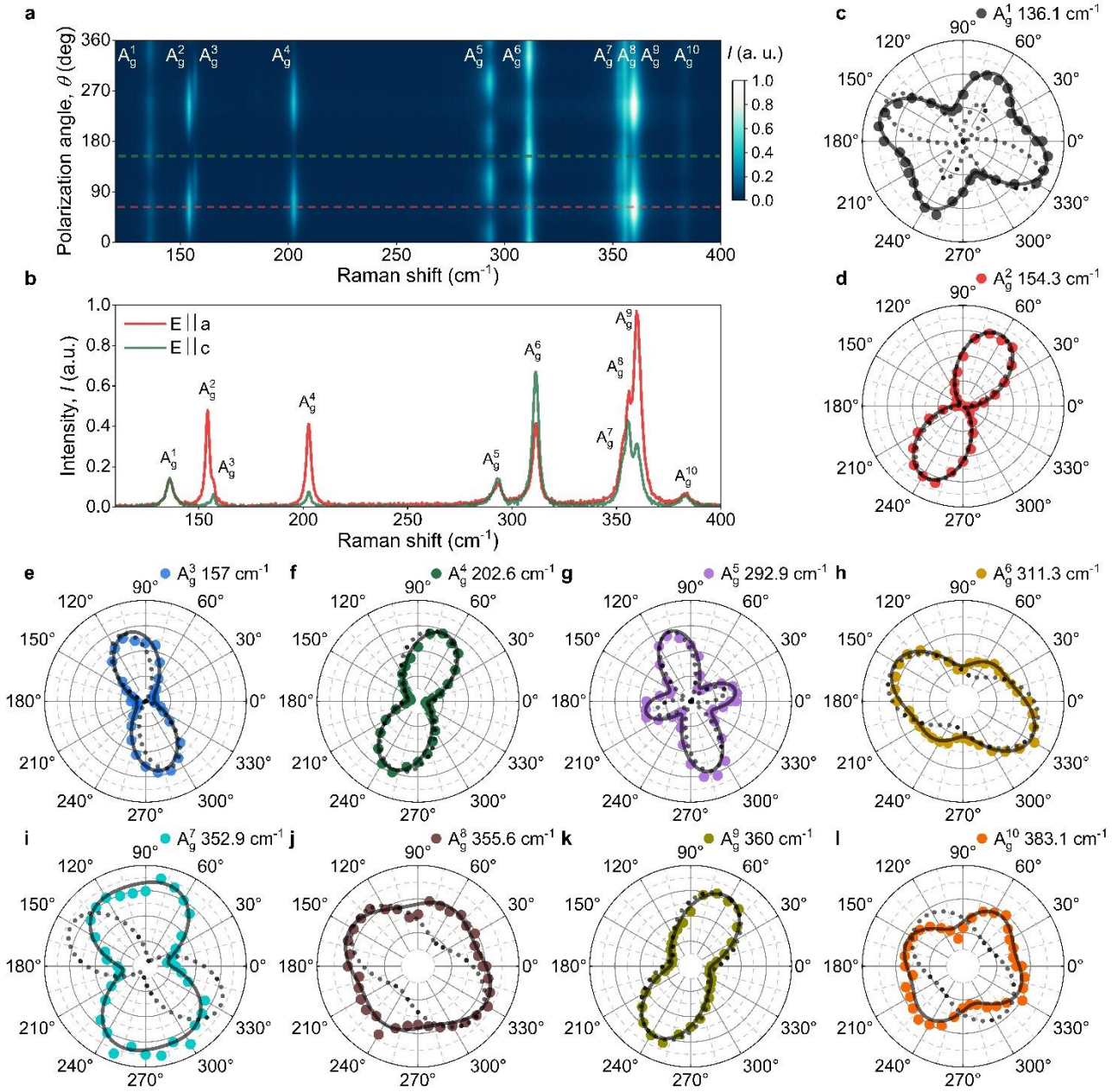

Supplementary Figure 9. (a) Angle-resolved Raman intensity colormap of a bulk As_2S_3 flake (thickness, $t \approx 310$ nm) acquired by rotating a sample in parallel-polarized configuration. Colored dashed lines indicate crystallographic directions. (b) Raman spectra along green and red lines on the map (a). (c-l) Polar plots of the normalized Raman intensity spectra for ten Raman modes. Dotted lines correspond to Raman calculations. The data in polar diagrams are normalized to their maximum values, respectively.

Supplementary Note 4: Processing of polarization-dependent transmittance spectra for As_2S_3

To determine optical axes position relative to the crystallographic axes, we performed micro-transmission measurements for the sample in parallel-polarized regime (see Methods). While the polarizer and the analyzer were fixed, we rotated the sample by 360° with a step of 5° and recorded the transmittance spectrum in the wavelength region of 500-850 nm for each angle. Supplementary Figure 8 shows the transmittance color map which contains spectra for all rotation angles. Next, we linearly approximated the extracted experimental spectra over intervals $\Delta\lambda$ of 1 nm and fitted them as follows:

$$T(\theta) = (E/E_0)^2 = \left|a(cos\ \theta)^2 + b(sin\ \theta)^2 e^{i\Delta\varphi}\right|^2 =$$

$$= a^2(cos\ \theta)^4 + b^2(sin\ \theta)^4 + 2ab(cos\ \theta)^2(sin\ \theta)^2 cos\ \Delta\varphi$$

where $T(\theta)$ are transmittance at a given wavelength λ and polarization angle θ, $\Delta\varphi$ is the phase retardance. We used the fitted curves to experimentally detect optical axes orientation.

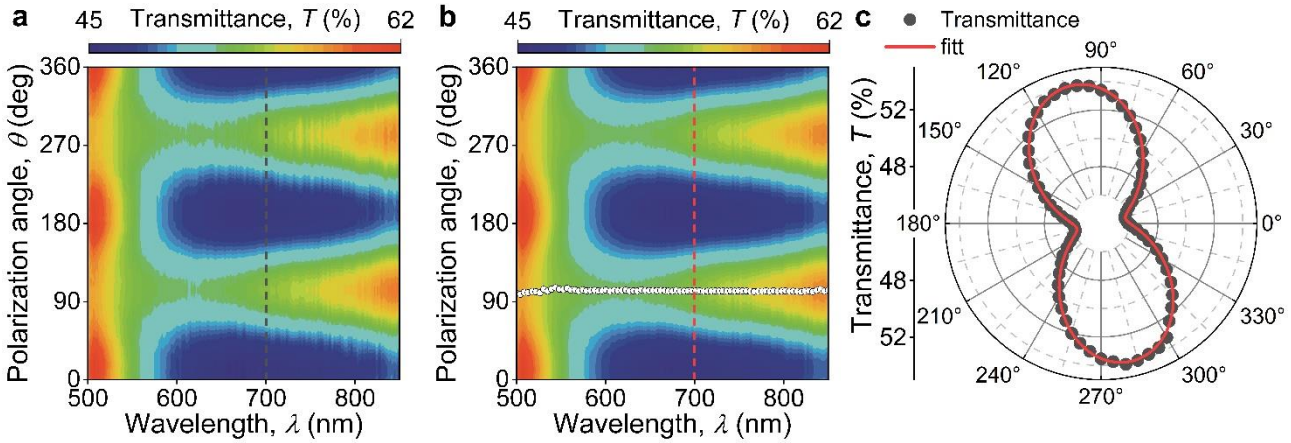

Supplementary Figure 10. (a,b) Polarized micro-transmittance experimental and fitting maps of 60-nm-thick As_2S_3 flake. (c) Angle-dependent transmittance diagram is taken along dashed lines in the panels (a,b).

Supplementary Note 5: Mueller matrix ellipsometry analysis for determination of As_2S_3 optical constants

In order to obtain the full dielectric tensor of As_2S_3 we recorded Mueller matrix in 5° step sample rotation over 180° at 550 nm using Accurion nanofilm_ep4 ellipsometer. The resulted optical constants from the fitting of Mueller matrix (Supplementary Figure 11) are plotted in Figure 3 of the main text.

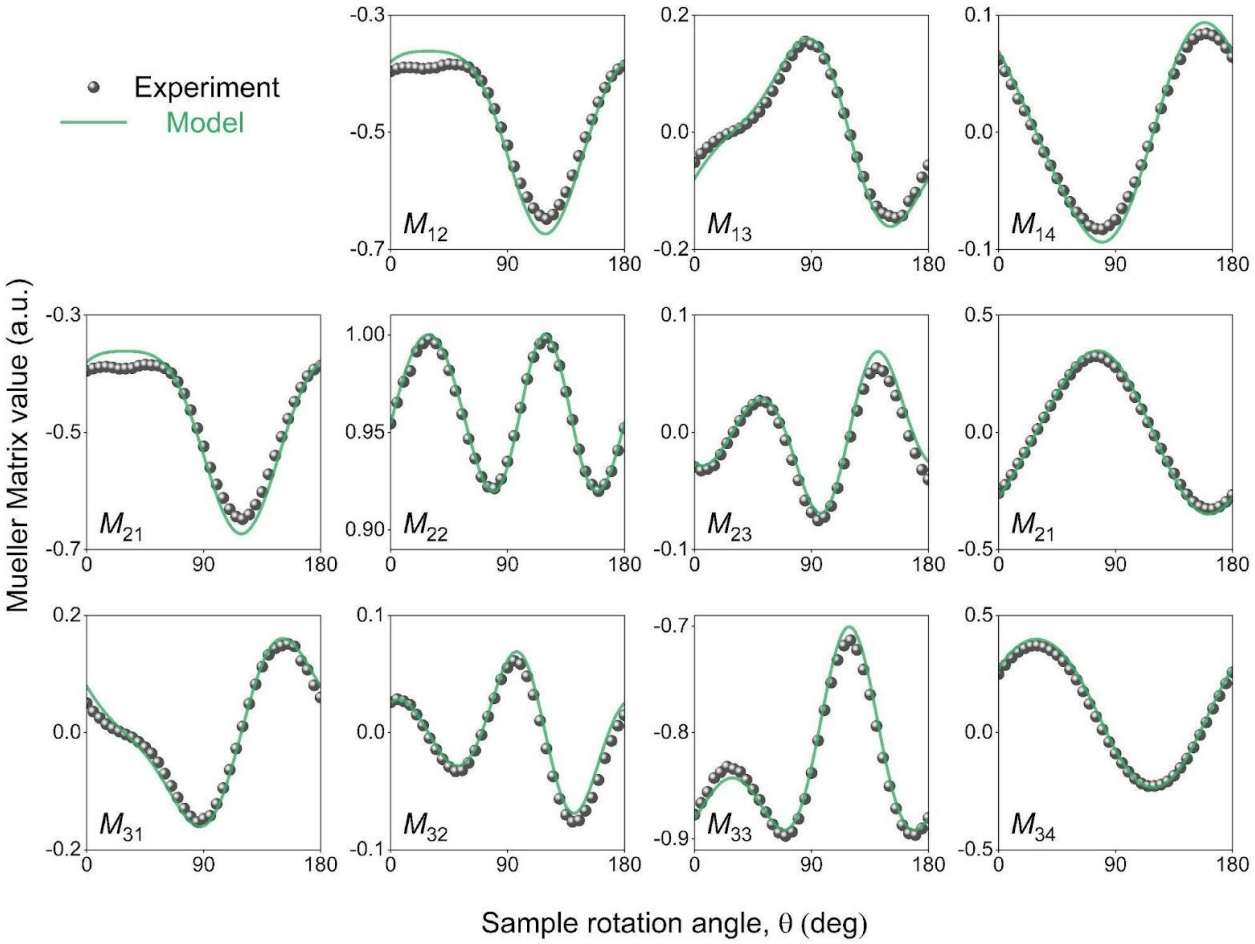

Supplementary Figure 11. Mueller matrix for As_2S_3.

Supplementary Note 6: Scanning near-field optical microscopy of As_2S_3

For near-field measurements, we exfoliated the flake of the required thickness ($h \approx 250$ nm) on Schott glass substrate. The thickness was determined so that only the fundamental TM mode could exist in the flake and there were no TM modes of higher orders. The measurements were carried out in the reflection mode. Meaning, the illumination of the sample and the collection of near-field information were performed by the same parabolic mirror. Since the material has an in-plane anisotropy of optical properties, we studied modes propagating in different directions as shown in Supplementary Figure 12. The shift of the observed oscillation frequency described by Hu and coauthors[17] was calculated from the shift of the air mode (effective mode index $n \approx 1.02$), which was observed in all measurements. To determine the refractive index of the material along the *b* axis n_b, we calculated the dispersion of planar TM_0 modes at various refractive indices n_b and fixed n_a and n_c taken from the results of the polarized micro-transmittance (described in the main text).

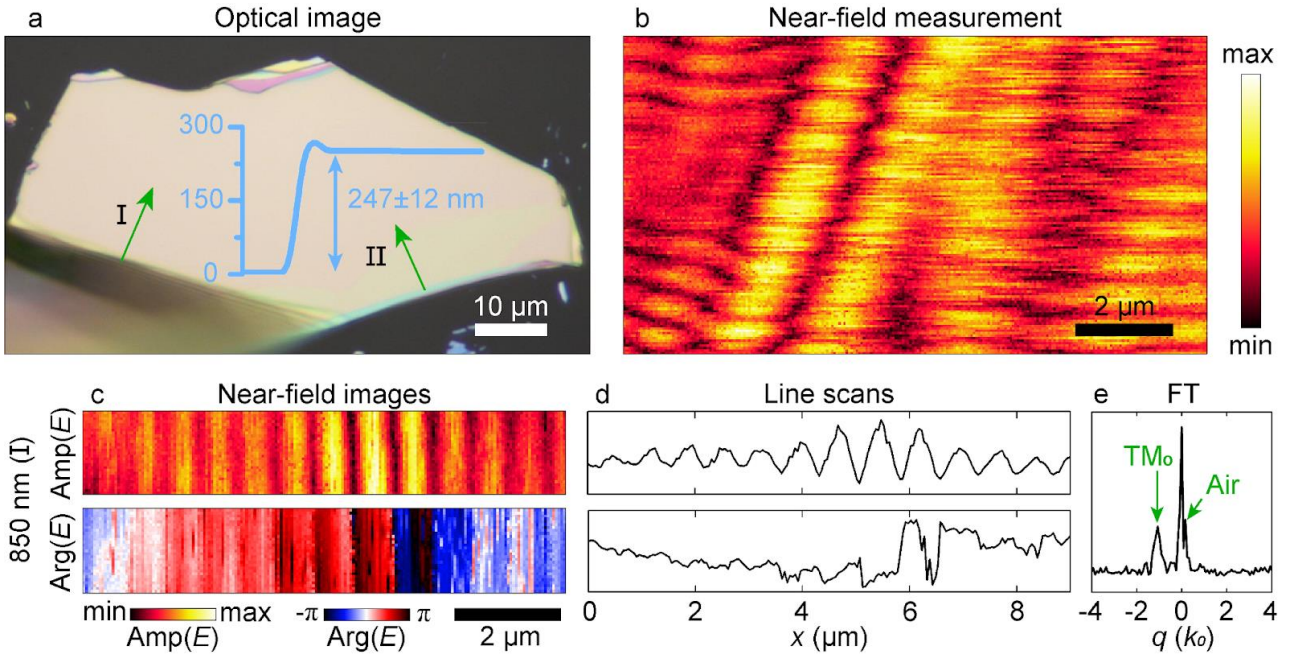

f Experimental results

Direction and wavelength	Effective mode index
700 nm (I)	1.91
700 nm (II)	1.96
850 nm (I)	1.74

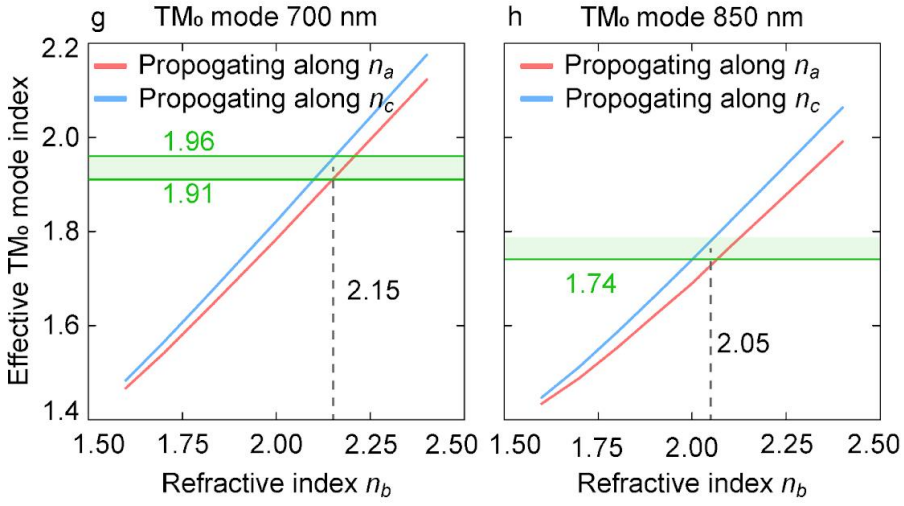

Supplementary Figure 12. Near-field analysis of As_2S_3. (a) Optical image of the analyzed As_2S_3 flake. The inset shows AFM height profile. Green lines show propagation directions of studied planar mode. (b) Standard near-field image of the desired region. (c) Near-field image, amplitude Amp(*E*) and phase Arg(*E*), of the electric field *E* taken at 850 nm along direction I. (d) *x*-line scans taken from panel (c) and averaged over 1.8 μm. (e) Fourier transform (FT) amplitude of the complex near-field signal in (d). (f) Table with correspondence between the propagation direction, wavelength and effective mode index. (g) and (h) effective mode index of the fundamental TM mode as a function of the refractive index of As_2S_3 along *b*-axis for modes propagating along *a*-axis (red) and *c*-axis (blue).

Supplementary Note 7: Tabulated optical constants of As_2S_3

Supplementary Table 4. Tabulated optical constants of As_2S_3.

λ (nm)	n_a (in-plane)	n_b (out-of-plane)	n_c (in-plane)
500	3.002	2.40425	3.38498
510	2.98205	2.38351	3.36294
520	2.96324	2.36395	3.34215
530	2.94548	2.34549	3.32253
540	2.9287	2.32804	3.30399
550	2.91283	2.31154	3.28646
560	2.8978	2.29591	3.26985
570	2.88355	2.2811	3.25411
580	2.87004	2.26704	3.23918
590	2.8572	2.2537	3.225
600	2.84501	2.24102	3.21152
610	2.8334	2.22895	3.1987
620	2.82236	2.21747	3.1865
630	2.81183	2.20653	3.17487
640	2.8018	2.19609	3.16378
650	2.79222	2.18614	3.15321
660	2.78308	2.17663	3.1431
670	2.77434	2.16755	3.13345
680	2.76599	2.15886	3.12422
690	2.758	2.15055	3.11539
700	2.75034	2.14259	3.10693
710	2.74301	2.13497	3.09883
720	2.73598	2.12766	3.09107
730	2.72924	2.12065	3.08362
740	2.72277	2.11392	3.07647
750	2.71656	2.10746	3.0696
760	2.71059	2.10126	3.06301
770	2.70485	2.09529	3.05667
780	2.69933	2.08955	3.05057
790	2.69402	2.08403	3.0447
800	2.6889	2.07871	3.03905
810	2.68398	2.07359	3.03361
820	2.67923	2.06866	3.02836
830	2.67466	2.0639	3.02331
840	2.67024	2.05931	3.01843
850	2.66599	2.05488	3.01373
860	2.66187	2.05061	3.00919
870	2.65791	2.04648	3.0048
880	2.65407	2.04249	3.00056
890	2.65036	2.03864	2.99647
900	2.64678	2.03491	2.99251

Supplementary Note 8: Transmittance calculations

In the experiment, incident light polarized by the first polarizer (P_1) falls normally at the flake of As_2S_3 placed on the glass substrate (Supplementary Figure 13). The transmitted light then passes through the measuring polarizer (analyzer) P_2. We measure the dependence of the light intensity on the mutual orientation of the sample and polarizers P_1 and P_2. For the theoretical computations of the transmission coefficient, we solve Maxwell's equations with appropriate boundary conditions.

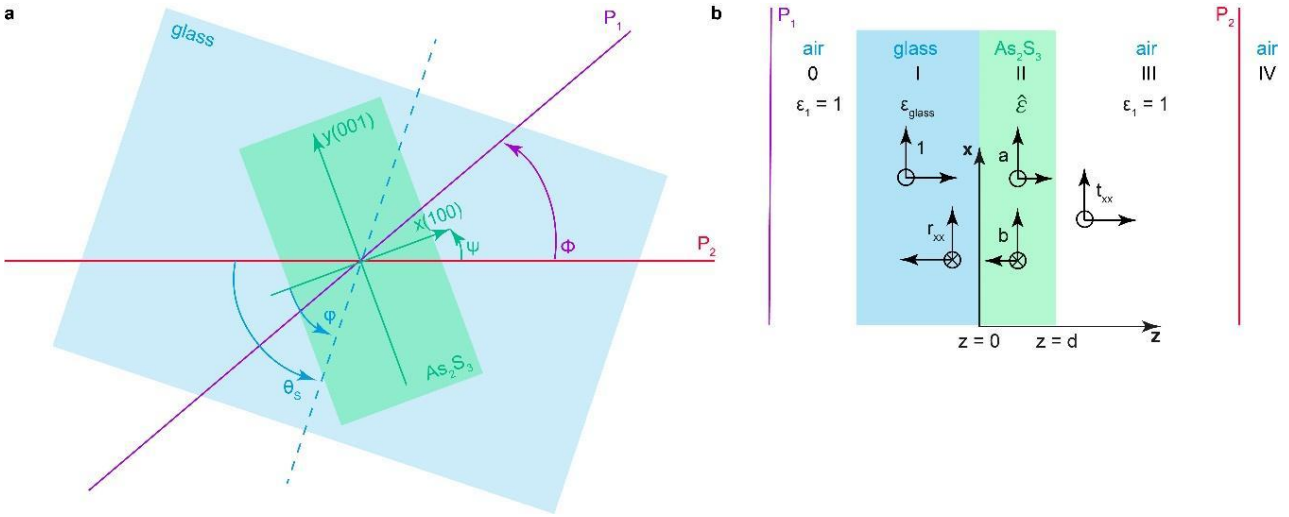

Supplementary Figure 13. Schematic top- and side-view of the experimental setup. (a) Angle arrangement of the As_2S_3 plate, the substrate and polarizers P_1 and P_2. (b) Field distribution (in-plane electric components, *E*, signed as narrows and out-of-plane magnetic components, *H*, signed as circles with and without "*x*" depending on the direction).

First, we find the electric field in the regions 0 - IV (see Figure 13b). Neglecting the back-reflections in the glass plate, we can write:

$$\mathbf{E}_{\mathrm{III}} = \hat{T}\mathbf{E}_{\mathrm{I}} = \hat{T}t_{\mathrm{air-glass}}\mathbf{E}_0, \tag{8.1}$$

where $\hat{T}$ is the Jones matrix describing the transmission through the As_2S_3 slab. In the basis of the principal directions of As_2S_3 dielectric permittivity tensor, the Jones vector of an incident light can be written as:

$$\mathbf{E}_0 = \begin{pmatrix} \cos(\phi-\theta) \\ \sin(\phi-\theta) \end{pmatrix}, \tag{8.2}$$

where θ is the angle between the *x*-axis of As_2S_3 and direction of the analyzer P_2, and ϕ is the angle between P_1 and P_2.

Since matrix $\hat{T}$ is diagonal, eq. (8.1) can be rewritten as:

$$\mathbf{E}_{\mathrm{III}} = t_{\mathrm{air-glass}} \begin{pmatrix} t_{xx}\cos(\phi-\theta) \\ t_{yy}\sin(\phi-\theta) \end{pmatrix} \tag{8.3}$$

To find the components of the transmission matrix we treat an As_2S_3 slab as a Fabry–Pérot resonator

$$t_{xx} = t^x_{\mathrm{I-II}}\Phi t^x_{\mathrm{II-III}} + t^x_{\mathrm{I-II}}\Phi r^x_{\mathrm{II-III}}\Phi r^x_{\mathrm{II-I}}\Phi t^x_{\mathrm{II-III}} + \cdots \tag{8.4}$$

where $t_{i-j} = 2n_i/(n_i + n_j)$, and $r_{i-j} = t_{i-j} - 1$ are the transmission and reflection amplitudes at the interface between regions *i* and *j* $(i, j = \mathrm{I}, \mathrm{II}, \mathrm{III})$ and $\Phi = \exp(ik_x d)$ is the phase accumulation factor which the wave with a wavenumber k_x acquires upon propagation through the slab of a thickness *d*. The superscript *x* above reflection and transmission amplitudes signifies that for their calculation we assume $n_{II} = n_x$.

Summation of an infinite geometric progression results in

$$t_{xx} = \frac{t^x_{\mathrm{I-II}} t^x_{\mathrm{II-III}} \exp(ik_x d)}{1 - r^x_{\mathrm{II-I}} r^x_{\mathrm{II-III}} \exp(2ik_x d)} \tag{8.5}$$

Similar equation with the trivial replacements is valid for t_{yy}.

The amplitude of the electric field of the detected wave after the analyzer P_2 is found by projecting the Jones vector onto the analyzer direction

$$E_{\mathrm{IV}} = t_{\mathrm{air-glass}}\big(t_{xx}\cos(\phi - \theta)\cos\theta - t_{yy}\sin(\phi - \theta)\sin\theta\big). \tag{8.6}$$

The transmission coefficient of our system reads:

$$T = \frac{|\mathbf{E}_{\mathrm{IV}}|^2}{|\mathbf{E}_0|^2} = |E_{\mathrm{IV}}|^2 \tag{8.7}$$

A few notes should be added regarding the measurement procedure. Spectrophotometer measures the ratio of the transmission through our system to the transmission of the reference system which consists only of the glass slab. So, the number given by eq. (8.7) should be divided by $|t_{\mathrm{air-glass}} t_{\mathrm{glass-air}}|^2$:

$$T_{\exp} = \frac{T}{|t_{\mathrm{air-glass}} t_{\mathrm{glass-air}}|^2}, \tag{8.8}$$

Furthermore, the orientation of the analyzer in our setup is fixed and unknown, therefore the experimental values of ϕ and θ differ from theoretical ones by a constant shift. However, by fitting the experimental data with eq. (8.8) we recover the orientation of the analyzer and, afterwards, the anisotropic refractive indices n_x and n_y of As_2S_3.

Supplementary Note 9: Quarter-waveplate based on As_2S_3

One of the main features of quarter-waveplates is their ability to transform a linearly polarized light into a circularly polarized. Assuming that $|t_{xx}|$ = *A* and $|t_{yy}|$ = *B*, we can rewrite the Jones vector after the As_2S_3 slab as:

$$E_{III} = t_{air-glass}\left(A\cos(\varphi-\theta); Be^{i\delta}\sin(\varphi-\theta)\right)^T$$

, where $\delta = Arg\left(t_{yy}/t_{xx}\right)$ and the common phase is discarded. This Jones vector corresponds to the circularly polarized light only if the phase retardance $\delta = \pm\pi/2$ and $\tan(\varphi-\theta) = \pm A/B$. The δ can be expressed as:

$$\delta = \left(k_x - k_y\right)d + Arg\left(\frac{1 - r^y_{II-I}r^y_{II-III}e^{2ik_yd}}{1 - r^x_{II-I}r^x_{II-III}e^{2ik_xd}}\right)$$

The first term here is the commonly used expression for the phase retardance in waveplates whereas the second term is related to the repeated reflections inside As_2S_3 slab hence can be named "Fabry–Pérot phase accumulation".

For materials with weak in-plane optical anisotropy ny-nxnx, the second term is negligible and *A* = *B*. By contrast, a waveplate made from a material with a strong in-plane anisotropy exhibits noticeable linear dichroism (*A* ≠ *B*) and the Fabry–Pérot phase accumulation. These features must be properly addressed during the waveplate design and actual use. In particular, the waveplate can be thinner or thicker than predicted by the simple expression $\delta = \left(k_x - k_y\right)d$. Also, the polarization direction of an incident light should form an angle different from π/4 with the principal optical directions of the waveplate to be converted into circularly polarized light, i.e., $\varphi - \theta \neq \pi/4$.

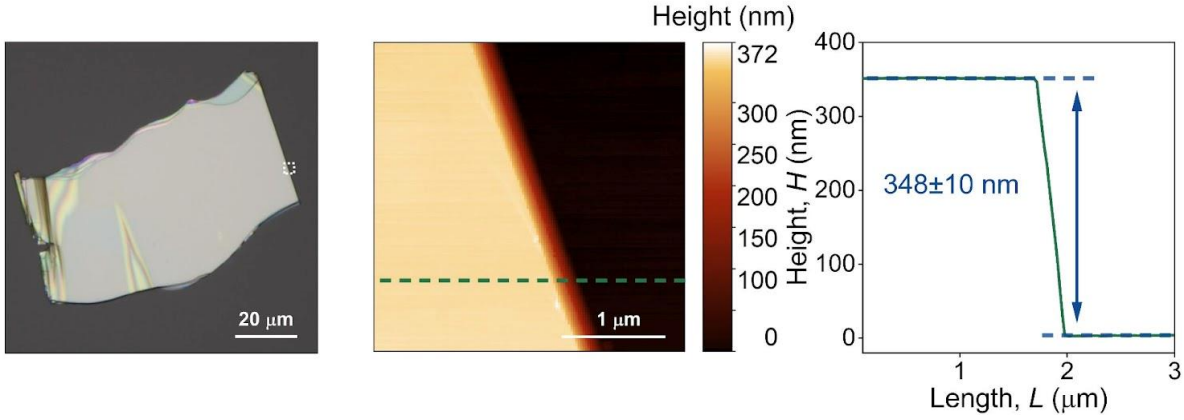

Supplementary Figure 14. AFM characterization of the As_2S_3 flake quarter-waveplate (t = 345 nm from transmitted data fitting). (a) Optical image of the As_2S_3 flake on Schott glass. (b) AFM topographical scan over the region marked by dashed rectangle in panel (a). (c) Cross-sectional profile along the green dashed line.

SUPPLEMENTARY REFERENCES

[1] N. MORIMOTO, *Mineral. J.* **1954**, *1*, 160.

[2] D. J. E. Mullen, W. Nowacki, *Zeitschrift für Krist.* **1972**, *136*, 48.

[3] J. P. Perdew, K. Burke, M. Ernzerhof, *Phys. Rev. Lett.* **1996**, *77*, 3865.

[4] J. Heyd, G. E. Scuseria, M. Ernzerhof, *J. Chem. Phys.* **2003**, *118*, 8207.

[5] G. Kresse, J. Furthmüller, *Phys. Rev. B* **1996**, *54*, 11169.

[6] G. Kresse, J. Furthmüller, *Comput. Mater. Sci.* **1996**, *6*, 15.

[7] M. Shishkin, G. Kresse, *Phys. Rev. B - Condens. Matter Mater. Phys.* **2006**, *74*, 1.

[8] A. Togo, F. Oba, I. Tanaka, *Phys. Rev. B* **2008**, *78*, 134106.

[9] A. Togo, I. Tanaka, *Scr. Mater.* **2015**, *108*, 1.

[10] A. Togo, L. Chaput, I. Tanaka, *Phys. Rev. B* **2015**, *91*, 094306.

[11] G. Kresse, J. Hafner, *Phys. Rev. B* **1993**, *47*, 558.

[12] S. Grimme, S. Ehrlich, L. Goerigk, *J. Comput. Chem.* **2011**, *32*, 1456.

[13] P. E. Blöchl, *Phys. Rev. B* **1994**, *50*, 17953.

[14] G. Kresse, D. Joubert, *Phys. Rev. B* **1999**, *59*, 1758.

[15] X. Gonze, J.-C. Charlier, D. C. Allan, M. P. Teter, *Phys. Rev. B* **1994**, *50*, 13035.

[16] X. Gonze, C. Lee, *Phys. Rev. B* **1997**, *55*, 10355.

[17] R. M. Pick, M. H. Cohen, R. M. Martin, *Phys. Rev. B* **1970**, *1*, 910.

[18] D. Hu, X. Yang, C. Li, R. Liu, Z. Yao, H. Hu, S. N. G. Corder, J. Chen, Z. Sun, M. Liu, Q. Dai, *Nat. Commun.* **2017**, *8*, 1471.